

QUASI-DISTRIBUTED NETWORK OF LOW-COHERENCE FIBER-OPTIC FABRY-PÉROT SENSORS WITH CAVITY LENGTH-BASED ADDRESSING

Katarzyna Karpienko, Marcin J. Marzejon, Adam Mazikowski, and Jerzy Pluciński

Gdańsk University of Technology, Faculty of Electronics, Telecommunications and Informatics, Department of Metrology and Optoelectronics, 11/12 Gabriela Narutowicza St., 80-233 Gdańsk, Poland (katkarip@pg.edu.pl, ✉ marcin.marzejon@pg.edu.pl, +48 58 347 1584, adamazik@pg.edu.pl, jerpluc@pg.edu.pl).

Abstract

Distributed measurement often relies on sensor networks. In this paper, we present the construction of low-coherence fiber-optic Fabry-Pérot sensors connected into a quasi-distributed network. We discuss the mechanism of spectrum modulation in this type of sensor and the constraints of assembly of such sensors in the network. Particular attention was paid to separate the signals from individual sensors which can be achieved by cavity length-based addressing. We designed and built a laboratory model of a temperature sensors network. The employed sensors are low-coherence Fabry-Pérot interferometric sensors in a fiber-optics configuration. The extrinsic sensor cavity utilizes the thermal expansion of ceramics, and the sensors are addressed by the different lengths of the cavities. The obtained test results show that the signal components from each sensor can be successfully separated, and the number of sensors could be expanded depending on the FWHM of the light source.

Keywords: Fabry-Pérot interferometer, sensors network, fiber-optics sensor, interferometry.

© 2020 Polish Academy of Sciences. All rights reserved

1. Introduction

Over the years, *fiber-optics sensors* (FOSs) have been employed in many metrological applications. They enable precise and high-resolution measurements of various physical quantities, among others: refractive index [1–3], displacement [4, 5], vibration [6, 7], strain [8, 9], pressure [10], temperature [11, 12], humidity [13], magnetic field [14], liquid level [15], and concentration of liquids [16]. In the very basic configuration, a FOS contains a light source, an optical fiber, a modulator, and a detection system [17]. Such a sensor uses the modulation of the light propagated in the fiber or an element of the fiber-optic path, to encode the information about the measurand.

Fiber-optics sensors are versatile in their applications. Both point and distributed measurements can be performed using FOSs, as well as quasi-distributed measurements when many of them are connected into a network [18–21]. FOSs are very small in size – the diameter of standard single-mode fiber is 125 microns. Also, they can be used for even very remote measurements. In such operation mode, the measurement signal is provided directly to the receiving system without conversion to an electrical signal, giving another advantage which is lack of risk of electric discharge. It enables applications for normally inaccessible areas and harsh environments, for instance, flammable substances extraction areas [19, 20].

The very common limitation of fiber-optic sensors-based measurement systems is the noise caused by time changes of the fiber-optics attenuation. This limitation can be overcome only for the particular types of FOSs. One of them are sensors for which the measurand changes the

21 spectrum of the signal. Examples of such sensors are low-coherence fiber-optics sensors (LC-
 22 FOS) for which the interference causes a change of the signal spectrum. Besides the ability to
 23 analyze the signal in the spectrum domain, LC-FOS can be easily miniaturized and applied in,
 24 *e.g.*, ultra-low-volume samples, or fast-changing parameters measurements dependent on the
 25 sensor time constant [22, 23].

26 The low-coherence fiber-optic sensors with a Fabry-Pérot cavity are well described in the
 27 literature and still explored for new applications and improved performance [24, 27]. There are
 28 reports about FOSs with Fabry-Pérot cavities made with nanosecond or femtosecond lasers [28,
 29 29], lateral offset splicing [30], cavities created during the fiber splicing process [31], or using
 30 different types of fiber-optic, *e.g.* hollow core or microstructured optical fibers [5, 32]. For
 31 instance, in 2019, Marta Nespereira *et al.* proposed a refractive index sensor with a Fabry-Pérot
 32 cavity manufactured in standard single-mode telecommunication fiber using nanosecond-pulse
 33 NIR Q-switched Nd:YAG laser [29]. In so prepared Fabry-Pérot cavity, its length was adjusted
 34 by a cleaver. For the proposed constructions, the sensor enables measurements with sensitivity
 35 up to $0.31 \text{ nm}^{-1}/\text{RIU}$ using later analysis, or $54 \text{ dB}/\text{RIU}$ using fringe visibility analysis. Another
 36 reported solution utilizes a capillary for in-fiber Fabry-Pérot cavity manufacturing [31]. So
 37 prepared strain sensor enables very-high sensitivity measurements ($7.53 \text{ pm}/\mu\epsilon$) for a cavity
 38 length of $2.189 \mu\text{m}$. The main disadvantage of the mentioned solutions is the complicated and
 39 expensive process of Fabry-Pérot cavity manufacturing, requiring sophisticated equipment and
 40 training.

41 In this work, we proposed a low-coherence fiber-optic sensor with an extrinsic Fabry-Pérot
 42 cavity, placed at the end of the fiber and connected with a low-coherence measurement system.
 43 We chose this particular design because of, among others, the possibility of sensor
 44 miniaturization even down to hundreds of microns. In our solution, the standard SMF-28 optical
 45 fiber, or another type of fiber can be employed, which significantly decreases the time and cost
 46 of producing such a sensor. Moreover, sensors can be connected to form a network enabling
 47 simultaneous measurements at many points. The use of sensors with the Fabry-Pérot cavity
 48 operating in a sensor network is a new concept that requires a solution to the problem of
 49 addressing these sensors. The paper proposes a method of addressing them, which has been
 50 theoretically analyzed and tested experimentally. For a correctly designed sensor network, the
 51 proposed signal analysis enables to obtain separated signals from all sensors.

52 2. Low-coherence interferometric sensors with extrinsic Fabry-Pérot cavities

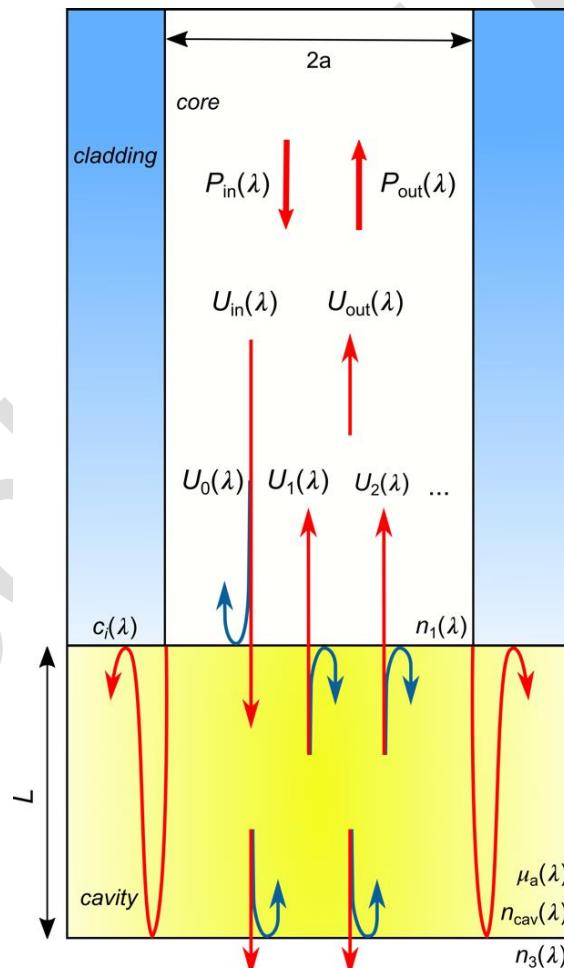
53 2.1. Principle of operation

54 The principle of operation of low-coherence interferometric sensors with extrinsic Fabry-
 55 Pérot cavities is based on measurement of the reflection (or transmission) spectrum of radiation
 56 propagated through or reflected from the cavity located at the end of the optical fiber. If the
 57 measurand changes this spectrum (*e.g.* as a result of a change in the Fabry-Pérot cavity length
 58 or refractive index of the substance filling the cavity), then, by its analysis, the measurand value
 59 can be determined. Since the optical radiation reflected from the Fabry-Pérot cavity can be
 60 treated as the sum of many interfering beams coming out of the cavity, the amplitude spectral
 61 density at the sensor output is equal to the sum of the amplitude spectral density of individual
 62 beams, so the power spectral density $P_{\text{out}}(\lambda)$ of radiation at the output of the sensor can be
 63 determined as:

$$64 \quad P_{\text{out}}(\lambda) = |U_{\text{out}}(\lambda)|^2 = \left| \sum_{i=0}^{\infty} U_i(\lambda) \right|^2, \quad (1)$$

65 where $U_{\text{out}}(\lambda)$ is amplitude spectral density of radiation reflected from the Fabry-Pérot cavity,
66 $U_0(\lambda)$ is amplitude spectral density of radiation that reflected from the boundary surface
67 between the end of optical fiber and the cavity, and $U_i(\lambda)$ (for $i > 0$) are the amplitude spectral
68 densities of beams that propagated at the distance equal to $2iL$ inside the cavity (where L is the
69 length of the cavity) and next were coupled to the optical fiber, and λ is the wavelength in a
70 vacuum (note that the amplitude spectral densities $U_{\text{out}}(\lambda)$ and $U_i(\lambda)$ are complex functions and
71 describe the radiation inside the optical fiber – see Fig. 1).

72 Contrary to classic Fabry-Pérot interferometers, which use interference of an infinite number
73 of planar waves propagated between two parallel mirrors, fiber optic sensors with extrinsic
74 Fabry-Pérot cavities use interference of an infinite number of non-planar waves derived from
75 the beam outgoing from the end of the optical fiber. A detailed analysis of the operation of these
76 sensors taking into account effects such as the diffraction phenomenon of the optical radiation
77 beam inside the cavity, the phase shift caused by the Gouy effect (the Gouy effect means an
78 additional slight phase shift of the wave compared to a plane wave of the same frequency as the
79 distance from the wave source increases; in the case of a Gaussian beam, this shift increases
80 from zero to $\pi/2$ as the distance increases from zero to infinity from the beam waist), and the
81 coupling coefficients $c_i(\lambda)$ of the waves from the cavity that are transmitted through the interface
82 between the cavity and the core of the optical fiber is presented in [33, 34].
83



84
85

Fig. 1. Optical radiation propagating in the fiber-optic sensor with the extrinsic Fabry-Pérot cavity.

86 When the coefficient of reflection of the boundary surfaces between the optical fiber and the
87 cavity or between the cavity and the center located behind the cavity is much smaller than 1,

88 then the amplitude spectral densities $U_i(\lambda)$ for $i > 1$ are negligibly small (compared with $U_0(\lambda)$
89 or $U_1(\lambda)$) and then the dependence (1) will take the form

$$90 \quad P_{\text{out}}(\lambda) = |U_0(\lambda) + U_1(\lambda)|^2. \quad (2)$$

91 Amplitude spectral density $U_0(\lambda)$ can be determined directly from the Fresnel equation
92 describing the ratio of reflected wave amplitude spectral density to the incident wave amplitude
93 spectral density at the boundary of two media:

$$94 \quad U_0(\lambda) = r_{12}(\lambda)U_{\text{in}}(\lambda), \quad (3)$$

95 where $U_{\text{in}}(\lambda)$ is the amplitude spectral density of the incident beam at the Fabry-Pérot cavity,
96 $r_{12}(\lambda)$ is the complex amplitude reflectance at the interface between the optical fiber and the
97 cavity:

$$98 \quad r_{12}(\lambda) = \frac{n_1(\lambda) - n_{\text{cav}}(\lambda)}{n_1(\lambda) + n_{\text{cav}}(\lambda)}, \quad (4)$$

99 and $n_1(\lambda)$ and $n_{\text{cav}}(\lambda)$ are the refractive indices of the fiber core and the medium inside the cavity,
100 respectively.

101 Determining amplitude spectral density $U_1(\lambda)$ is slightly more complicated than determining
102 amplitude spectral density $U_0(\lambda)$. Apart from the Fresnel phenomenon, one should also take into
103 account the phenomenon of diffraction causing the beam to widen inside the cavity and
104 changing the wavefront radius of curvature of the beam, the attenuation of the beam inside the
105 cavity, the phase shift proportional to the distance that beam propagates inside the cavity, the
106 Gouy effect causing an additional phase shift of the beam, $\zeta_1(\lambda)$, and coupling of the beam
107 coming out of the cavity with the beam propagating in the core of the optical fiber. Taking all
108 these phenomena into account, $U_1(\lambda)$ can be determined as

$$109 \quad U_1(\lambda) = t_{12}(\lambda)r_{23}(\lambda)t_{21}(\lambda)\sqrt{T_{\text{cav}}(\lambda)}\exp\left(-j\frac{4\pi Ln_{\text{cav}}(\lambda)}{\lambda}\right)\exp[j\zeta_1(\lambda)]c_1(\lambda)U_{\text{in}}(\lambda), \quad (5)$$

110 where $t_{12}(\lambda)$ and $t_{21}(\lambda)$ are the complex amplitude transmittances at the interface between the
111 optical fiber and the cavity from the optical fiber to the cavity and from the cavity to the optical
112 fiber, respectively:

$$113 \quad t_{12}(\lambda) = 1 + r_{12}(\lambda), \quad (6)$$

$$114 \quad t_{21}(\lambda) = 1 - r_{12}(\lambda). \quad (7)$$

115 $T_{\text{cav}}(\lambda)$ is the power transmittance in the cavity at the distance of $2L$:

$$116 \quad T_{\text{cav}}(\lambda) = \exp[-2L\mu_a(\lambda)], \quad (8)$$

117 where L is the length of the cavity, $\mu_a(\lambda)$ and $n_{\text{cav}}(\lambda)$ are the absorption coefficient and the
118 refractive index of the medium that fills the cavity, respectively, and $c_1(\lambda)$ is the complex
119 coupling coefficient of the beam coming out of the cavity with the beam propagating in the core
120 of the optical fiber which includes a mismatch of diameters of beams outgoing from the cavity
121 and propagating in the core of the optical fiber and curvatures of the wavefronts of these beams.

122 For a step-index single-mode optical fiber, the beam propagating inside the cavity can be
123 approximated by a Gaussian beam for which [33]

$$124 \quad \exp[j\zeta_1(\lambda)]c_1(\lambda) = \frac{2\pi n_{\text{cav}}(\lambda)w_0^2(\lambda)}{2\pi n_{\text{cav}}(\lambda)w_0^2(\lambda) - j2L\lambda}, \quad (9)$$

125 where $w_0(\lambda)$ is the fundamental mode field radius and L is the cavity length.
 126 By substituting (3) and (5) into (2), we finally obtain

$$127 \quad P_{\text{out}}(\lambda) = P_0(\lambda) + P_1(\lambda) + 2\sqrt{P_0(\lambda)P_1(\lambda)} \cos[\Delta\varphi(\lambda)], \quad (10)$$

128 where:

$$129 \quad P_0(\lambda) = |U_0(\lambda)|^2 = R_{12}(\lambda)P_{\text{in}}(\lambda), \quad (11)$$

130 and

$$131 \quad P_1(\lambda) = |U_1(\lambda)|^2 = R_{23}(\lambda)[1 - R_{12}(\lambda)]^2 T_{\text{cav}}(\lambda) \frac{[2\pi n_{\text{cav}}(\lambda)w_0^2(\lambda)]^2}{[2\pi n_{\text{cav}}(\lambda)w_0^2(\lambda)]^2 + (2L\lambda)^2} P_{\text{in}}(\lambda) \quad (12)$$

132 are the power spectral densities of the beams that are reflected at the interface between the
 133 optical fiber and the cavity and the interface between the cavity and the medium behind the
 134 cavity, respectively, $R_{12}(\lambda)$ and $R_{23}(\lambda)$ are the power reflectances ($R_{12}(\lambda) = |r_{12}(\lambda)|^2$ and $R_{23}(\lambda) =$
 135 $|r_{23}(\lambda)|^2$), $P_{\text{in}}(\lambda)$ is power spectral density of the beam incident on the cavity and

$$136 \quad \Delta\varphi(\lambda) = \varphi_1(\lambda) - \varphi_0(\lambda) \quad (13)$$

137 is the phase difference between the phase shifts of the beams reflected at the interfaces between
 138 the cavity and the medium behind the cavity, $\varphi_1(\lambda)$, and between the optical fiber and the cavity,
 139 $\varphi_0(\lambda)$, relative to the incident beam phase.

140 If $n_1 > n_{\text{cav}}$, $\varphi_0(\lambda) = 0$, otherwise $\varphi_0(\lambda) = \pi$. The phase shift $\varphi_1(\lambda)$ is the sum of the phase shift
 141 associated with covering the distance in the cavity by the beam, $\varphi_{1L}(\lambda) = 2\pi L n_{\text{cav}}(\lambda)/\lambda$, the phase
 142 shift associated with the reflection, $\varphi_{1R}(\lambda)$, and the total shift associated with the coupling and
 143 the Gouy effect, $\varphi_{1cG}(\lambda)$ (i.e. $\varphi_{1cG}(\lambda)$ includes the phase shift caused by the curvature of the
 144 wavefront of the beam outgoing from the cavity, $\varphi_{1c}(\lambda)$, and the phase shift caused by Gouy
 145 effect, $\varphi_{1G}(\lambda)$: $\varphi_{1cG}(\lambda) = \varphi_{1c}(\lambda) + \varphi_{1G}(\lambda)$. $\varphi_{1R}(\lambda) = 0$, if $n_{\text{cav}} > n_3$ or $\varphi_{1R}(\lambda) = \pi$, if $n_{\text{cav}} < n_3$. The phase
 146 shift $\varphi_{1cG}(\lambda)$ we can obtain as the argument of the right side of (9):

$$147 \quad \varphi_{1cG}(\lambda) = \arg \left[\frac{2\pi n_{\text{cav}}(\lambda)w_0^2(\lambda)}{2\pi n_{\text{cav}}(\lambda)w_0^2(\lambda) - j2L\lambda} \right] = \arctan \left[\frac{2L\lambda}{2\pi n_{\text{cav}}(\lambda)w_0^2(\lambda)} \right]. \quad (14)$$

148 As the Rayleigh range of the Gaussian beam inside the cavity is

$$149 \quad z_0(\lambda) = \frac{\pi n_{\text{cav}}(\lambda)w_0^2(\lambda)}{\lambda}, \quad (15)$$

150 the relationship (14) can be rewritten as:

$$151 \quad \varphi_{1cG}(\lambda) = \arctan \left[\frac{L}{z_0(\lambda)} \right]. \quad (16)$$

152 In a special case, when $n_1 > n_{\text{cav}}$ and $n_{\text{cav}} < n_3$, from (13) we obtain

$$153 \quad \Delta\varphi(\lambda) = 2\pi L n_{\text{cav}}(\lambda)/\lambda + \pi + \arctan \left[\frac{L}{z_0(\lambda)} \right]. \quad (17)$$

154 Note that the total phase shift associated with the coupling and the Gouy effect,
 155 $\varphi_{1cG}(\lambda) = \arctan[L/z_0(\lambda)]$, is smaller than the phase shift caused only by the Gouy effect,
 156 $\varphi_{1G}(\lambda) = \arctan[2L/z_0(\lambda)]$.

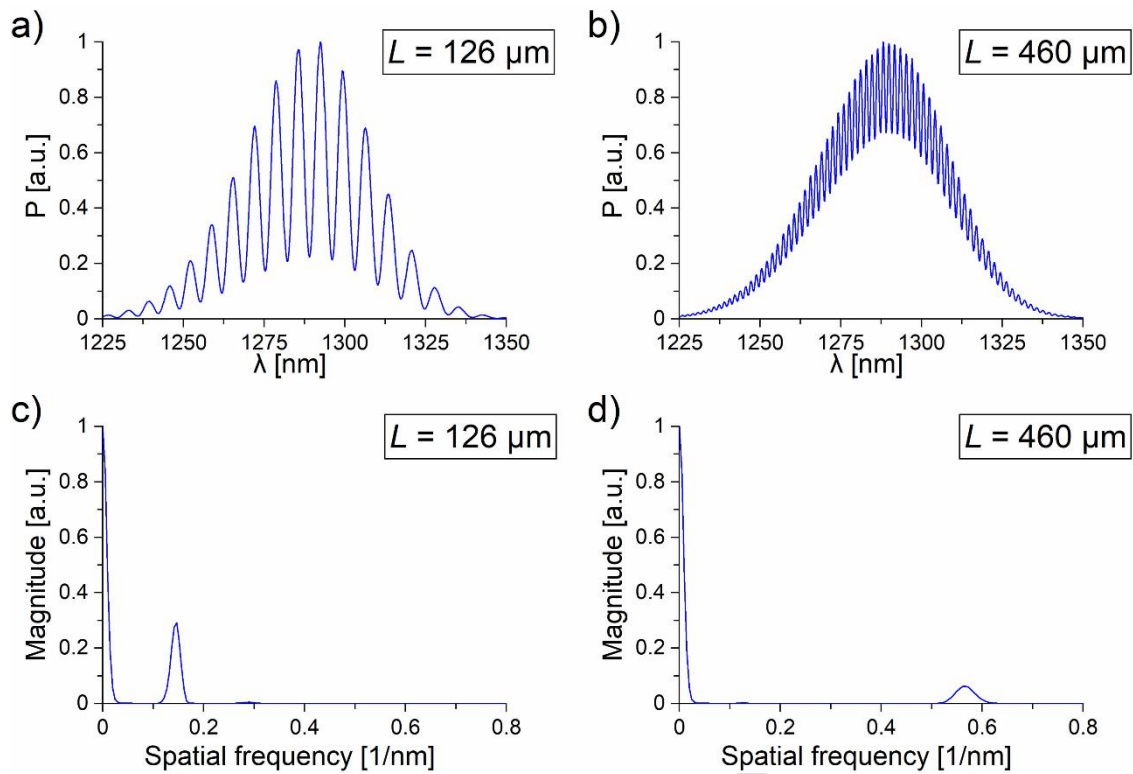
157

158 **2.2. Using sensors in the sensor network**

159 The key aspect of using a given type of sensor to build a sensor network is the separation of
160 measurement signals derived from individual sensors so that signals from one sensor do not
161 interfere with signals from other sensors. One of the most frequently used signal separation
162 methods in networks is based on wavelength-division multiplexing of the optical signal. Each
163 sensor modulates the transmission of radiation in a narrow wavelength band with a different
164 center wavelength. This method is applied *e.g.* in sensor networks using Bragg gratings.
165 Another well-known signal separation method is the use of measurement of the time of flight
166 of optical signals from the radiation source to sensors and back by the optical time-domain
167 reflectometry (OTDR) or frequency-domain reflectometry (OFDR) systems [35, 36]. The
168 mentioned systems are applied in intensity modulation fiber-optic sensor networks.

169 Since low-coherence interferometric sensors with extrinsic Fabry-Pérot cavities modulate
170 the power of the optical signal over a very wide range of wavelengths, more advanced methods
171 are needed to separate the signals from these sensors connected to the sensor network than the
172 methods used in the sensor networks mentioned above. The problem is that any sensor using
173 the Fabry-Pérot cavity modulates the signal over the entire wavelength range of the radiation
174 source used in the sensor network which does not allow for the separation of signals from
175 individual sensors with the use of narrowband optical filters or signal analysis from an optical
176 spectrum analyzer measuring the level and position of spectral lines of the optical signal at the
177 output of a sensor network (as is the case in sensor networks using *e.g.* Bragg gratings). The
178 fact that the spectrum modulation rate changes with cavity length (see (10), (13), and (17)) can
179 be used to separate the measurement signals derived from individual low-coherence
180 interferometric sensors with extrinsic Fabry-Pérot cavities. For example, Fig. 2 a) and b) present
181 examples of calculated power spectrum densities at the output of sensors that use an empty
182 cavity formed by two end surfaces of single-mode type SMF-28 optical fibers (a refractive
183 index of the core equal to 1.452, core diameter equal to 8.2 μm , and mode field diameter equal
184 to 9.2 μm at 1290 nm [37, 38]) for a cavity length of 126 μm and 460 μm . It was assumed that
185 the profile of the radiation beam coming from the optical fiber can be approximated by
186 a Gaussian beam with the waist diameter equal to the fundamental-mode size width [33, 39].
187 This diameter is equal to 8.5 μm at 1290 nm which is less than the mode field diameter
188 (provided by manufacturers of optical fibers according to the Petermann II mode field diameter
189 definition). In calculations, it was assumed that the sensors were excited by the radiation source
190 having a Gaussian spectrum distribution with a central wavelength $\lambda_0 = 1290$ nm and a spectral
191 width $\Delta\lambda = 50$ nm at FWHM. The densities and their Fourier transforms are shown in Fig. 2 c)
192 and d).

193



194

195
 196
 197
 198
 199
 200

Fig. 2. Calculated power spectral densities at the output of sensors and the Fourier transforms of these power spectral densities. It was assumed that the sensors use an empty cavity formed by two end surfaces of single-mode type SMF-28 optical fibers for a cavity length of 126 μm (a) and 460 μm (b), and the radiation source has a Gaussian spectrum distribution with the central wavelength $\lambda_0 = 1290$ nm and spectral width at FWHM $\Delta\lambda = 50$ nm. The Fourier transforms of calculated power spectrum densities for a cavity length of 126 μm and 460 μm are shown in Fig. (c) and (d), respectively.

201
 202
 203
 204
 205
 206
 207
 208
 209
 210
 211
 212
 213

Each Fourier transforms shown in Fig. 2 c) and d) has two components: the first component depends on the spectrum of the radiation source only, while the second one depends on both: the spectrum of the radiation source and the spectrum modulation rate. In sensor networks, the latter component can be used to measure changes in the length of the cavity on the basis of which the measured quantity is measured. In the case of multiple sensors, these components could be separated by filtering if they do not overlap. Assuming the Gaussian distribution of the radiation source and assuming the same distributions of beams reflected from the cavity (with the accuracy of a constant factor) and also assuming that the phase shift $\Delta\varphi(\lambda)$ is proportional to the length of the cavity (by neglecting the Gouy effect – see (17)), the dispersion of the glass from which the optical fiber is made, and the mode field diameter dependence on the wavelength), it can be shown from (10) that it is possible to filter the above-mentioned components if the minimum difference in the length of the cavities of individual sensors, ΔL_{\min} , satisfies the relationship [40, 41]:

214

$$\Delta L_{\min} = \frac{2 \cdot \ln 2}{\pi} \frac{\lambda_0^2}{\Delta\lambda} \quad (18)$$

215
 216
 217
 218
 219
 220
 221

It was assumed in (1) that individual components of the Fourier transform can be separated if they are separated by a value equal to at least their length. In practice, to avoid crosstalk between signals coming from individual sensors, having different signal levels, and taking into account neglected effects when determining the relationship (18), the differences in the length of the cavities of individual sensors should be minimum twice the calculated value ΔL_{\min} . For example, for $\lambda_0 = 1290$ nm and $\Delta\lambda = 50$ nm, from (18) we obtain $\Delta L_{\min} = 14.7$ μm which means that the differences in lengths of the cavities of individual sensors in the sensor network should

222 be not smaller than approximately 30 μm . If we assume that the shortest Fabry-Pérot cavity
 223 length should exceed 30 μm (i.e. so that main spectrum components can be separated from the
 224 constant component resulting from the Fourier transform – see Fig. 2 c)), and the longest should
 225 not exceed e.g. 0.5 mm (the maximum length of the cavity depends on many factors, including
 226 the resolving power measurement of the spectrum and the adopted required depth of spectrum
 227 modulation), we obtain that the maximum number of sensors connected in the network is 16.
 228 This number is directly proportional to the spectrum width of the broadband light source to be
 229 used. The 50 nm width of light results from available, relatively cheap broadband sources using
 230 super luminescence diodes. If it is necessary to build a network consisting of a greater number
 231 of sensors, sources using several super luminescence diodes with different central wavelengths,
 232 or much more expensive sources using the generation of supercontinuum or broadly tunable
 233 lasers can be used. The latter two types of sources are available and widely used in frequency-
 234 domain optical coherence tomography (FD-OCT) [42–44].

235 3. Experiment

236 The design of a low-coherence interferometric sensor with extrinsic Fabry-Pérot cavity
 237 length-based addressing is schematically shown in Fig. 3. In this construction, the first
 238 interferometer mirror is the polished end face of the single-mode SMF-28 optical fiber, ended
 239 with FC/PC connector. The second mirror is the end face of the single-mode SMF-28 optical
 240 fiber which is placed in a flat polished ferrule. Both mirrors are positioned by using a brass
 241 sleeve. Another advantage of such a solution is the possibility to change the Fabry-Pérot cavity
 242 length through the spreading or narrowing of mirrors relative to each other. However, due to
 243 the design difficulties related mainly to problems in carrying out an accurate reference
 244 measurement of the Fabry-Pérot cavity length, significantly different cavity length were set for
 245 both sensors, despite calculating the minimum difference at 30 μm .

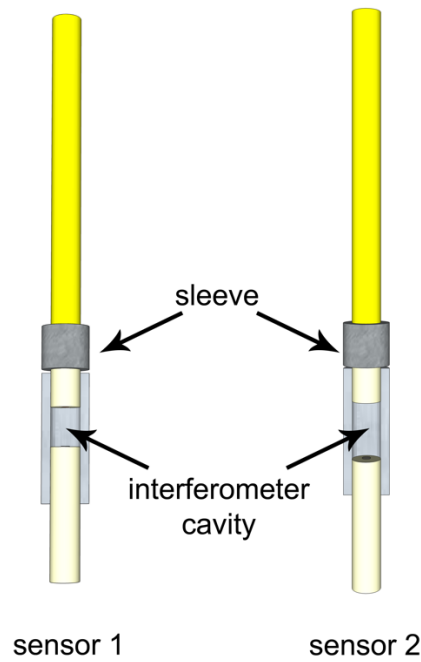
246 The sensor was designed for temperature measurements. The thermal expansion coefficients
 247 of ferrules and sleeves are about $0.5 \cdot 10^{-6}/^{\circ}\text{C}$ and $17 \cdot 10^{-6}/^{\circ}\text{C}$, respectively. Since the thermal
 248 expansion coefficients of ferrules and optical fibers are relatively very small and very similar,
 249 the cavity length changes due to temperature change primarily depended on the linear thermal
 250 expansion of the sleeves. On the other hand, a high difference in thermal coefficients of ferrules
 251 and the sleeve can cause a mutual shift of these elements as a result of stress caused by
 252 temperature changes. However, as the experiments showed (see Section 4), the measurements
 253 are repeatable, therefore, the mentioned shift can be neglected.

254 Assuming no shift between the ferrule and the sleeve, and a very little thermal expansion
 255 coefficient of the ferrule (negligible in comparison to thermal expansion coefficient of the
 256 sleeve), the length change of the cavity ΔL is a product of the air gap length L_0 (that can be
 257 bigger than the Fabry-Pérot cavity length due to cut edges of the front faces of ferrules) and the
 258 thermal expansion coefficient of the sleeve α :

$$259 \quad \Delta L = L_0 + \alpha \cdot T, \quad (19)$$

260 where T is a temperature.
 261





262
263
264

Fig. 3. The idea of a low-coherence interferometric sensor with extrinsic Fabry-Pérot cavity length-based addressing.

265 4. Sensor network

266 4.1. Network topology

267 Several network topologies can be applied to optical fiber-based sensor networks. The most
268 popular ones are a bus, a dual bus (also called a ladder), and a star. In this work, we proposed
269 a sensor network using the star topology. The easiest way to create such a network is to couple
270 N sensors with a $1 \times N$ fiber-optic coupler. For an ideal star-topology sensor network, the power
271 of the light source is divided into each of the sensors in ratio $1/N$ (when the coupler splits the
272 power evenly). If needed, the optical power for each sensor can be adjusted using couplers with
273 different couple ratios r . The star topology has an important advantage – new sensors can be
274 added or removed without disturbing the sensors, making the network easy to scale. Also, if
275 one sensor breaks down, it does not affect other sensors.

276 The use of couplers in the network allows for far-reaching network optimization from the
277 point of view of the level of the received signal from individual sensors, *e.g.* couplers with
278 a division different than 50:50 can be used. The use of couplers, although it complicates the
279 construction of the network, is particularly beneficial if individual sensors show large losses
280 (that is, if the sum of the power of radiation reflected from and transmitted by the Fabry-Pérot
281 interferometer and then transmitted in the core of the optical fiber is much smaller than the
282 power of radiation falling on the interferometer). It can take place, *e.g.*, if the cavity length is
283 greater than the Rayleigh range of the beam subject to the phenomenon of diffraction inside the
284 interferometer cavity. In such case, big losses result from the fact that part of the radiation
285 power instead of further propagation in the fiber core is lost in the cavity. The phenomenon of
286 diffraction and its consequences can be omitted in sensors with very short cavities (*i.e.* shorter
287 than the Rayleigh range). In this situation, it is possible to build a quasi-assembled sensor
288 consisting of a series of fiber optic-wire cells.

289 In general, it can be said that the design of networks consisting of low-coherence fiber optic
290 sensors using external Fabry-Pérot interferometers is much more difficult, especially in relation
291 to networks consisting of sensors with Bragg networks. The latter can be designed to have very

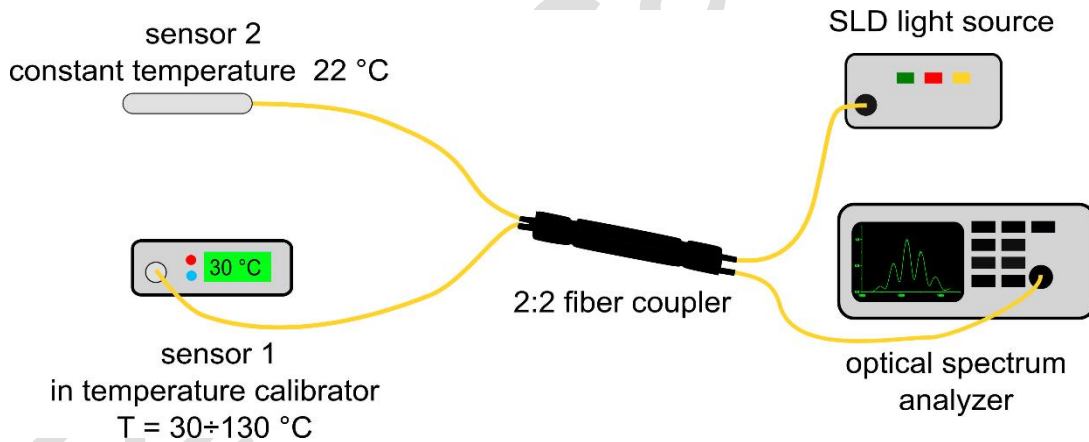
292 low losses. Moreover, they show very selective reflection for radiation of a specific wavelength
 293 (for which Bragg condition is met) and very high transmission for other wavelengths. Radiation
 294 that has not been reflected from the Bragg grating can be used for other sensors with another
 295 fixed network in the Bragg grating. Such possibilities are not provided by low-coherence fiber
 296 optic sensors with Fabry-Pérot interferometer, where the reflected and transmitted radiation is
 297 modulated over the entire spectrum of the radiation source and which often show much higher
 298 losses.

299 The output signal is a superposition of the signals from each sensor in the network.
 300 Therefore, a crucial thing is to keep the sensor signal modulated individually for each network
 301 component. If not, signal recovery from a particular sensor will be impossible.

302 4.2. Measurement setup

303 To experimentally prove the idea of a low-coherence fiber-optics sensors network,
 304 a dedicated laboratory setup was built. The setup consists of two low-coherence sensors
 305 (described in 3.1) for temperature measurements, whose cavities were equal to 126 μm and
 306 460 μm , a superluminescent diode (S1300-G-I-20 by Superlum, Ireland), and an optical
 307 spectrum analyzer (AQ6319 by ANDO, Japan), all connected with the 2x2 single-mode fiber
 308 coupler (coupling ratio 50:50). Moreover, a temperature calibrator (ETC-400A by Ametek,
 309 USA) was used for temperature changes. It ensures high-temperature stability at the level of
 310 ± 0.15 $^{\circ}\text{C}$ (application note [45]). The sensors of the developed network are completely
 311 independent, that is, they allow the simultaneous measurement of two different temperatures.
 312 The measurement setup is presented in Fig. 4.

313



314

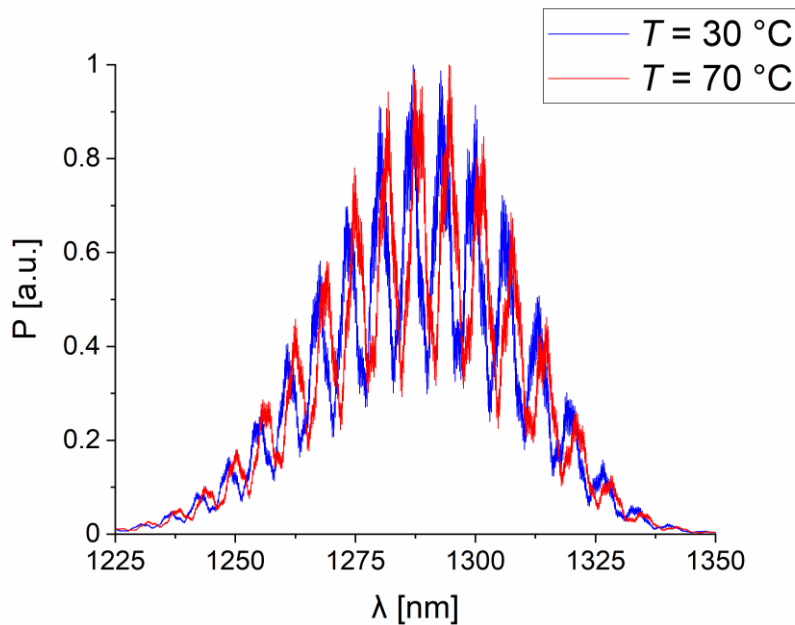
315

Fig. 4. Measurement setup.

316 The optical spectrum analyzer could be replaced by a much faster and cheaper optical
 317 spectrometer, using a diffraction grating and a CCD or CMOS detector matrix. Such a solution
 318 reduces the data acquisition time up to 5 orders of magnitude. A similar approach is applied in
 319 Spectral Domain Optical Coherent Tomography (SD-OCT) systems, where it enables data
 320 acquisition at a frequency of tens of kilohertz. Unfortunately, because of the number of detector
 321 pixels, the spectral resolution of such a solution is lower than the spectral resolution of an optical
 322 spectrum analyzer. For now, the most promising way to reduce the cost of the setup and keep
 323 the high precision and resolution of the measurement seems to be the use of the tunable laser.

324 For verification of the operation of the sensor network, several measurements have been
 325 taken. It had been decided, that during the experiment, one of the sensors was kept at the
 326 constant temperature of 22 $^{\circ}\text{C}$, while the temperature of the other sensor was increased and
 327 decreased in the range from 30 $^{\circ}\text{C}$ to 130 $^{\circ}\text{C}$, with 10 $^{\circ}\text{C}$ steps. The measurement signal from

328 both sensors was registered at the same time and on one interferogram. Selected interferograms
329 acquired during the measurements are presented in Fig. 5 as an example.
330

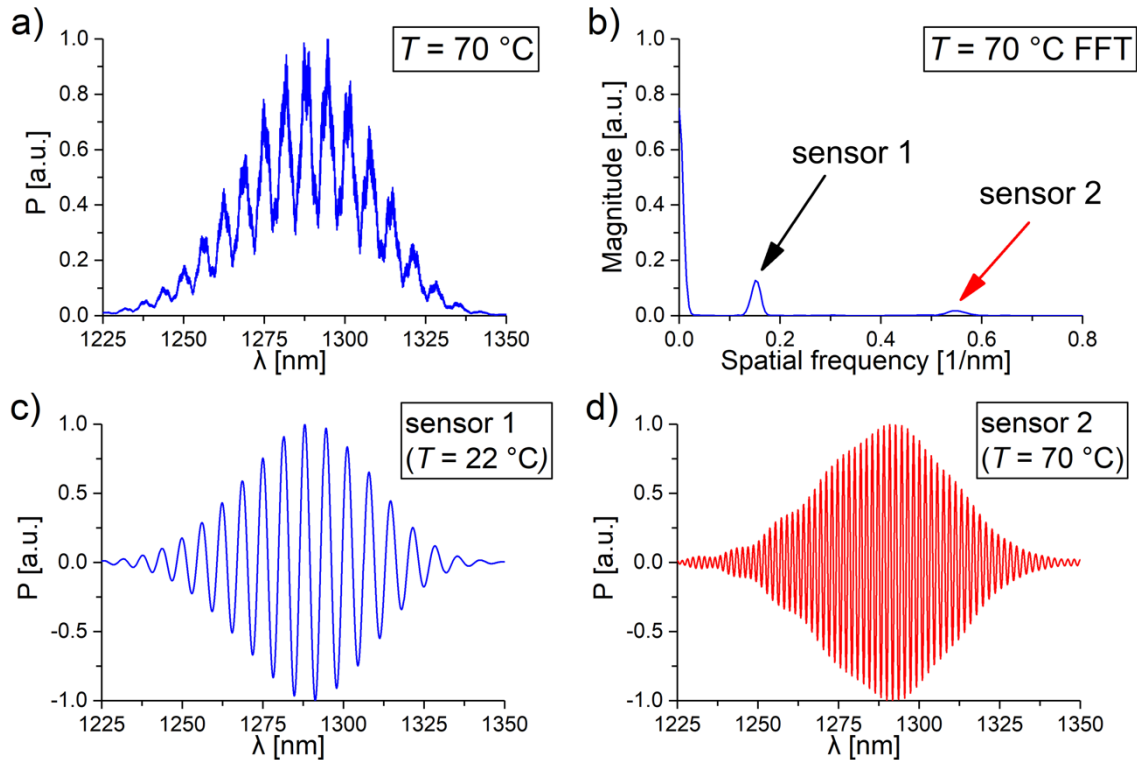


331
332 Fig. 5. Registered interferograms for temperatures equal to 30 °C and 70 °C for the sensor 1 heating cycle.

333 As shown, the interferograms acquired for a different temperature of at least one sensor vary.
334 Nevertheless, it is hard to extract information about the temperature for individual sensors of
335 the network. Thus, advanced signal processing is required.

336 4.3. Signal analysis

337 For the signal analysis, the Fourier transformation was employed. This operation enables to
338 separate signals from both sensors connected in the network. The selected interferogram
339 acquired during the measurements and its Fourier transform are presented in Fig. 6.
340



341

342 Fig. 6. Signal analysis of registered interferograms. a) Registered interferogram for the temperature of 70 °C for
 343 the sensor 1 heating cycle. b) Fourier transform of registered interferogram with components of sensors 1 and 2
 344 marked with a black and red arrow, respectively. c) Calculated interferogram for the temperature of 70 °C for
 345 heating cycle for sensor 1. d) Calculated interferogram for the temperature of 70 °C for heating cycle for sensor
 346 2.

347 For each acquired interferogram, the Fourier transform was calculated using the MATLAB
 348 built-in `fft()` function. The acquired interferogram was padded with trailing zeros to length
 349 2048, and then Fourier transform was calculated. Since the SLD source has Gaussian spectral
 350 characteristics, no windowing function was applied. As shown in Fig. 6 b), the Fourier
 351 transform of the acquired signal consists of the component depending on the spectrum of the
 352 radiation source only (the DC component with a spatial frequency close to 0) and components
 353 depending on both the spectrum of the radiation source and the spectrum modulation rate (the
 354 sensor components). Due to the selected parameters of sensors cavities lengths, the sensor
 355 components of the spectrum are well separated in the spatial frequency domain. The main
 356 spectrum component from sensor 1 is marked with the black arrow, whereas the main spectrum
 357 component from sensor 2 is marked with the red arrow in Fig. 6 b).

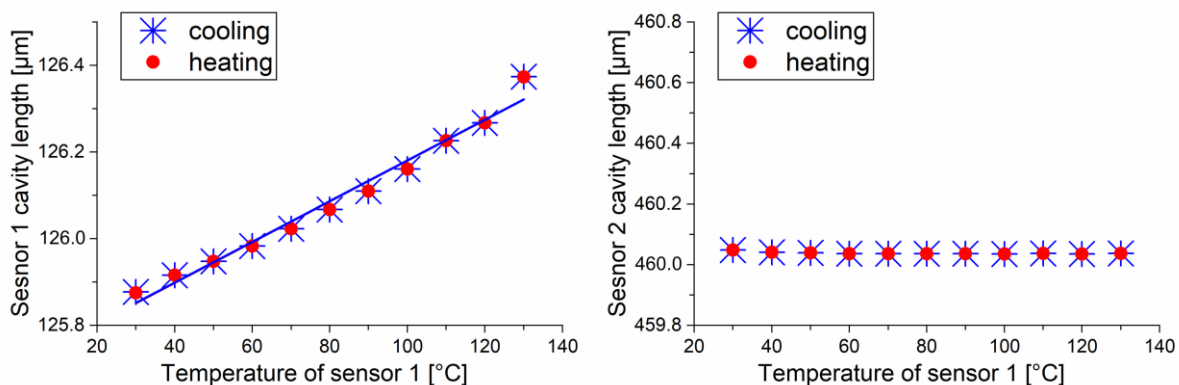
358 To obtain information about the spectrum fringes separation, the inverse Fourier transform
 359 of the signal components was employed. The inverse Fourier transform was calculated using
 360 the MATLAB built-in `ifft()` function. The length of the computed interferogram was kept the
 361 same as the length of the acquired interferogram, i.e., equal to 2001. For each sensor, only the
 362 main components were taken into account. Also, the DC component was omitted because of
 363 the impossibility of its separation. Due to that, the shape of the processed interferogram is quite
 364 different from the original one. The processed interferograms (for sensor 2 temperature equal
 365 to 70 °C) for both sensors are shown in Fig. 6 c) and d). For separated sensor interferograms,
 366 the number of maxima is higher for sensor 2 whose temperature is higher than for sensor 1. It
 367 is in line with our expectations – the length of the sensor 1 cavity is smaller than that of sensor
 368 2 which influences the length of the optical path in the interferometer cavity. Therefore, for
 369 sensor 2, the number of maxima in the calculated interferogram is higher than the number of
 370 maxima in the calculated interferogram for sensor 1. Moreover, the maximum wavelength

371 values for sensor 2 in various temperature conditions are different – the temperature is higher,
372 the maximum wavelength is red-shifted.

373 4.4. Results

374 The analysis described in Section 4.3 was performed for each acquired interferogram, and
375 the calculated interferograms (see Fig. 6 c) and d)) were analyzed. Then, using the fitting
376 method based on the developed software, the sensor cavity length was determined for each
377 performed measurement.

378 The analysis in the function of temperature above was performed for both sensors of the
379 network. We observed dependence between the cavity length wavelength corresponding to the
380 obtained signal interferogram and the temperature calibrator reading. The cavity lengths of both
381 sensors as the function of temperature are presented in Fig. 7 a) and b), respectively.
382



383
384 Fig. 7. Relationship between the maximum wavelength position in the function of temperature.

385 For sensor 1, we observed an increase of the calculated cavity length while temperature
386 increased. The obtained data were fitted with a linear function with a very high determination
387 coefficient R^2 value equal to 0.976. Apart from minor changes in the interferograms for the
388 same temperature between heating and cooling cycles, the calculated cavity length remained
389 the same. Assuming that the output value of the system is the calculated cavity length, the slope
390 of the characteristic (sensor temperature sensitivity) can be estimated as 4.70 nm/°C.

391 5. Summary

392 In this paper, we proposed a fiber-optic sensor network using low-coherence interferometric
393 sensors with extrinsic Fabry-Pérot cavities. We validated the network both numerically and
394 experimentally. The signals from individual sensors can be easily separated using a Fourier
395 transform. The proposed solution requires only one broadband light source with wavelengths
396 lying in the transmission band of the optical fiber. These wavelengths should be longer than the
397 cut-off wavelength of the optical fiber. The spectrum width of this source has a significant
398 impact on the maximum number of sensors that can be used in the network so that signals from
399 these sensors can be separated. Theoretically, more sensors in the network could be used for a
400 wider spectrum. So far, only models of temperature sensors have been used in the work to check
401 the possibility of building a network of fiber optic sensors using external Fabry-Pérot cavities.
402 For practical applications, these sensors should be miniaturized. In the miniaturized version,
403 the use of these sensors in the network can be particularly attractive for monitoring
404 infrastructure in the power industry (e.g. transmission lines or cables) due to the possibility of
405 transmitting measurement signals over a long distance in the presence of strong electromagnetic

406 interference. Sensors of this type can be particularly attractive if dielectrics (*e.g.* ceramics) are
 407 used instead of metal elements for their construction. Another potential application area for a
 408 network of these sensors could be the monitoring of pipelines, highways, and any other structure
 409 requiring remote measurements over long-distance. After meeting the requirements for the
 410 accumulation of electrostatic charge, these sensors can also be used in mines and the
 411 petrochemical industry.

412 Although the described concept has been validated based on the temperature sensor network,
 413 the conclusions can be extended to networks of sensors of other physical quantities, if their
 414 operation is based on an interference sensor with Fabry-Pérot cavity.

415 Acknowledgments

416 This research work was supported by the DS program of the Faculty of Electronics,
 417 Telecommunications and Informatics, Gdańsk University of Technology, and the TASK
 418 Academic Computer Centre in Gdańsk, Poland

419 References

- 420 [1] Tian, J., Lu, Y., Zhang, Q., & Han, M. (2013). Microfluidic refractive index sensor based on an all-silica in-
 421 line Fabry-Perot interferometer fabricated with microstructured fibers. *Optics Express*, 21(5), 6633–6639.
 422 <https://doi.org/10.1364/OE.21.006633>
- 423 [2] Liao, C. R., Hu, T. Y., & Wang, D. N. (2012). Optical fiber Fabry-Perot interferometer cavity fabricated by
 424 femtosecond laser micromachining and fusion splicing for refractive index sensing. *Optics Express*, 20(20),
 425 22813–22818. <https://doi.org/10.1364/OE.20.022813>
- 426 [3] Selvas-Aguilar, R., Castillo-Guzman, A., Cortez-Gonzalez, L., Toral-Acosta, D., Martinez-Rios, A., Anzueto-
 427 Sanchez, G., Duran-Ramirez, V. M., & Arroyo-Rivera, S. (2016). Noncontact Optical Fiber Sensor for
 428 Measuring the Refractive Index of Liquids. *Journal of Sensors*, 2016, 1–6.
 429 <https://doi.org/10.1155/2016/3475782>
- 430 [4] Marzejon, M., Karpieńko, K., Mazikowski, A., & Jędrzejewska-Szczerska, M. (2019). Fibre-optic sensor for
 431 simultaneous measurement of thickness and refractive index of liquid layers. *Metrology and Measurement*
 432 *Systems*, 26(3), 561–568. <https://doi.org/10.24425/mms.2019.129584>
- 433 [5] Harun, S. W., Yang, H. Z., Arof, H., & Ahmad A. (2012). Theoretical and experimental studies on coupler-
 434 based fiber optic displacement sensor with concave mirror. *Optik*, 123(23), 2105–2108.
 435 <https://doi.org/10.1016/j.ijleo.2011.10.006>
- 436 [6] Zhang, Q., Zhu, T., Hou, Y., & Chiang, K. S. (2013). All-fiber vibration sensor based on a Fabry-Perot
 437 interferometer and a microstructure beam. *Journal of the Optical Society of America B*, 20(5), 1211–1215.
 438 <https://doi.org/10.1364/JOSAB.30.001211>
- 439 [7] Kim, D. H., Han, J. H., & Lee, I. (2005). Vibration Measurement and Flutter Suppression Using Patch-type
 440 EFPI Sensor System. *International Journal of Aeronautical and Space Sciences*, 6(1), 17–26.
 441 <https://doi.org/10.5139/IJASS.2005.6.1.017>
- 442 [8] Jiang, M., & Gerhard, E. (2001). A simple strain sensor using a thin film as a low-finesse fiber-optic Fabry-
 443 Perot interferometer. *Sensors and Actuators A: Physical*, 88(1), 41–46. [https://doi.org/10.1016/S0924-4247\(00\)00494-5](https://doi.org/10.1016/S0924-4247(00)00494-5)
- 444 [9] Yang, F., Wang, Z. K., & Wang, D. N. (2019). A highly sensitive optical fiber strain sensor based on cascaded
 445 multimode fiber and photonic crystal fiber. *Optical Fiber Technology*, 47, 102–106.
 446 <https://doi.org/10.1016/j.yofte.2018.11.029>
- 447 [10] Dai, L., Wang, M., Cai, D., Rong, H., Zhu, J., Jia, S., & You, J., (2013). Optical Fiber Fabry-Pérot Pressure
 448 Sensor Based on a Polymer Structure. *IEEE Photonics Technology Letters*, 25(24), 2505–2508.
 449 <https://doi.org/10.1109/LPT.2013.2287289>
- 450 [11] Du, Y., Qiao, X., Rong, Q., Yang, H., Feng, D., Wang, R., Hu, M., & Feng, Z. (2014). A Miniature Fabry-
 451 Pérot Interferometer for High Temperature Measurement Using a Double-Core Photonic Crystal Fiber. *IEEE*
 452 *Sensors Journal*, 14(4), 1069–1073. <https://doi.org/10.1109/JSEN.2013.2286699>



- 454 [12] Zhao, Y., Zhao, J., & Zhao, Q. (2020). High sensitivity seawater temperature sensor based on no-core optical
455 fiber. *Optical Fiber Technology*, 54. <https://doi.org/10.1016/j.yofte.2019.102115>
- 456 [13] Xu, W., Huang, W.-B., Huang, X.-G., & Yu, C. (2013). A simple fiber-optic humidity sensor based on
457 extrinsic Fabry-Perot cavity constructed by cellulose acetate butyrate film. *Optical Fiber Technology*, 19(6),
458 583–586. <https://doi.org/10.1016/j.yofte.2013.09.005>
- 459 [14] Lv, R.-Q., Zhao, Y., Wang, D., & Wang, Q. (2014). Magnetic Fluid-Filled Optical Fiber Fabry-Pérot Sensor
460 for Magnetic Field Measurement. *IEEE Photonics Technology Letters*, 26(3), 217–219.
461 <https://doi.org/10.1109/LPT.2013.2290546>
- 462 [15] Wang, W., & Li, F., (2014). Large-range liquid level sensor based on an optical fibre extrinsic Fabry-Perot
463 interferometer. *Optics and Lasers in Engineering*, 52, 201-205.
464 <https://doi.org/10.1016/j.optlaseng.2013.06.009>
- 465 [16] Lu, Y., Li, H., Qian, X., Zheng, W., Sun, Y., Shi, B., & Zhang Y. (2020). Beta-cyclodextrin based reflective
466 fiber-optic SPR sensor for highly-sensitive T detection of cholesterol concentration. *Optical Fiber*
467 *Technology*, 56, 102187-1–6. <https://doi.org/10.1016/j.yofte.2020.102187>
- 468 [17] Huang, Y. W., Tao, J., & Huang, X. G. (2016). Research Progress on F-P Interference-Based Fiber-Optic
469 Sensors. *Sensors (Switzerland)*, 16(9), 1424. <https://doi.org/10.3390/s16091424>
- 470 [18] Perez-Herrera, R. A., & Lopez-Amo, M. (2013). Fiber optic sensor networks. *Optical Fiber Technology*,
471 19(6), 689-699. <https://doi.org/10.1016/j.yofte.2013.07.014>
- 472 [19] Lönnermark, A., Hedekvist, P. O., & Ingason, H. (2008). Gas temperature measurements using fibre Bragg
473 grating during fire experiments in a tunnel. *Fire Safety Journal*, 43(2), 119–126.
474 <https://doi.org/10.1016/j.firesaf.2007.06.001>
- 475 [20] Huang, Y., Fang, X., Bevans, W. J., Zhou, Z., Xiao, H., & Chen, G. (2013). Large-strain optical fiber sensing
476 and real-time FEM updating of steel structures under the high temperature effect. *Smart Materials and*
477 *Structures*, 22(1). <https://doi.org/10.1088/0964-1726/22/1/015016>
- 478 [21] Kersey, A. D. (1996). A Review of Recent Developments in Fiber Optic Sensor Technology. *Optical Fiber*
479 *Technology*, 2(3), 291–317. <https://doi.org/10.1006/ofte.1996.0036>
- 480 [22] Márquez-Cruz, V. A., & Hernández-Cordero, J. A. (2014). Fiber optic Fabry-Perot sensor for surface tension
481 analysis. *Optics Express*, 22(3), 3028–3038. <https://doi.org/10.1364/OE.22.003028>
- 482 [23] Jędrzejewska-Szczerska, M. (2014). Response of a New Low-Coherence Fabry-Perot Sensor to Hematocrit
483 Levels in Human Blood. *Sensors (Switzerland)*, 14(4), 6965–6976. <https://doi.org/10.3390/s140406965>
- 484 [24] Li, M., Wang, S., Jiang, J., Liu, K., Yu, L., & Liu, T. (2020). Cryogen adaptive and integrated differential
485 pressure sensor for level sensing based on an optical Fabry-Perot interferometer. *Applied Optics*, 59(8), 2457–
486 2461. <https://doi.org/10.1364/AO.384293>
- 487 [25] Zhang, X., Wang, W., Chen, H., Tang, Y., Ma, Z., & Wang, K. (2019). Two-Parameter Elliptical Fitting
488 Method for Short-Cavity Fiber Fabry-Pérot Sensor Interrogation. *Sensors (Switzerland)*, 19(1), 36-1–11.
489 <https://doi.org/10.3390/s19010036>
- 490 [26] Wei, H., & Krishnaswamy, S. (2020). Adaptive fiber-ring lasers based on an optical fiber Fabry-Perot cavity
491 for high-frequency dynamic strain sensing. *Applied Optics*, 59(2), 530–535.
492 <https://doi.org/10.1364/AO.377368>
- 493 [27] Maciak, E. (2019). Low-coherence Interferometric Fiber Optic Sensor for Humidity Monitoring Based on
494 Nafion® Thin Film. *Sensors (Switzerland)*, 19(3). <https://doi.org/10.3390/s19030629>
- 495 [28] Liu, Y., & Qu, S. (2014). Optical fiber Fabry-Pérot interferometer cavity fabricated by femtosecond laser-
496 induced water breakdown for refractive index sensing. *Applied Optics*, 53(3), 469-474.
497 <https://doi.org/10.1364/AO.53.000469>
- 498 [29] Nespereira, M., Coelho, J. M. P., & Rebordão, J. M. (2019). A Refractive Index Sensor Based on a Fabry-
499 Perot Interferometer Manufactured by NIR Laser Microdrilling and Electric Arc Fusion. *Photonics*, 6(4).
500 <https://doi.org/10.3390/photonics6040109>
- 501 [30] Yang, Y., Wang, Y., Jiang, J., Zhao, Y., He, X., & Li, L. (2019). High-sensitive all-fiber Fabry-Perot
502 interferometer gas refractive index sensor based on lateral offset splicing and Vernier effect. *Optik (Stuttg)*,
503 196. <https://doi.org/10.1016/j.ijleo.2019.163181>

- 504 [31] Domínguez-Flores, C. E., Monzón-Hernández, D., Minkovich, V. P., Rayas, J. A., & Lopez- Cortes, D.
 505 (2020). In-Fiber Capillary-Based Micro Fabry-Perot Interferometer Strain Sensor. *IEEE Sensors Journal*,
 506 20(3), 1343–1348. <https://doi.org/10.1109/JSEN.2019.2948013>
- 507 [32] Shi, Q., Lv, F., Wang, Z., Jin, L., Hu, J.J., Liu, Z., Kai, G., & Dong, X. (2008). Environmentally Stable Fabry–
 508 Pérot-Type Strain Sensor Based on Hollow-Core Photonic Bandgap Fiber. *IEEE Photonics Technology*
 509 *Letters*, 20(4), 237–239. <https://doi.org/10.1109/LPT.2007.913335>
- 510 [33] Pluciński, J., & Karpienko, K. (2016). Fiber optic Fabry-Pérot sensors: modeling versus measurements results.
 511 *Proc. SPIE 10034, 11th Conference on Integrated Optics: Sensors, Sensing Structures, and Methods*,
 512 100340H. <https://doi.org/10.1117/12.2244578>
- 513 [34] Pluciński, J., & Karpienko, K. (2016). Response of a fiber-optic Fabry-Pérot interferometer to refractive index
 514 and absorption changes: modeling and experiments. *Proc. SPIE 10161, 14th International Conference on*
 515 *Optical and Electronic Sensors*, 101610F. <https://doi.org/10.1117/12.2247510>
- 516 [35] Pluciński, J., Wierzbza, P., & Kosmowski, B. B. (2005). Time-of-flight fiber optic sensors for strain and
 517 temperature measurement. *Proceedings of SPIE 5952, Optical Fibers: Applications*, 59521H.
 518 <https://doi.org/10.1117/12.622880>
- 519 [36] Engelbrecht, R. (2017). Fiber Optic Strain and Temperature Sensing: Overview of Principles. *B6 – Distributed*
 520 *and Fiber Bragg Grating Sensing I, Proceedings Sensor 2017*, Germany, 255–260.
 521 <https://doi.org/10.5162/sensor2017/B6.1>
- 522 [37] Corning (2014). *Corning® SMF-28® Ultra Optical Fiber*.
 523 <https://www.corning.com/media/worldwide/coc/documents/Fiber/SMF-28%20Ultra.pdf>
- 524 [38] Thorlabs (2020). Single Mode Fiber with Ø900 µm Hytrel Jacket – SMF-28-J9.
 525 [https://www.thorlabs.com/drawings/f9d1e4029c087698-2F8A4710-ABC5-FCD9-](https://www.thorlabs.com/drawings/f9d1e4029c087698-2F8A4710-ABC5-FCD9-3959641FC02B0330/SMF-28-J9-SpecSheet.pdf)
 526 [3959641FC02B0330/SMF-28-J9-SpecSheet.pdf](https://www.thorlabs.com/drawings/f9d1e4029c087698-2F8A4710-ABC5-FCD9-3959641FC02B0330/SMF-28-J9-SpecSheet.pdf)
- 527 [39] Marcuse, D. (1977). Loss analysis of single-mode fiber splices. *The Bell System Technical Journal* 56(5),
 528 703–718. <https://doi.org/10.1002/j.1538-7305.1977.tb00534.x>
- 529 [40] Bouma, B. E., & Tearney, G. J. (2002). *Handbook of Optical Coherence Tomography*. New York: Marcel
 530 Dekker.
- 531 [41] Drexler, W., & Fujimoto, J. G. (2015). *Optical Coherence Tomography: Technology and Applications* (2nd
 532 ed.). New York: Springer International Publishing.
- 533 [42] Strąkowski, M., Pluciński, J., & Kosmowski, B. B. (2011). Polarization sensitive optical coherence
 534 tomography with spectroscopic analysis. *Acta Physica Polonica A*, 120(4), 785–788.
 535 <https://doi.org/10.12693/APhysPolA.120.785>
- 536 [43] Strąkowski, M., Kraszewski, M., Trojanowski, M., & Pluciński, J. (2014). Time-frequency analysis in optical
 537 coherence tomography for technical objects examination. *Proceeding of SPIE 9132, Optical Micro- and*
 538 *Nanometrology V*, 91320N. <https://doi.org/10.1117/12.2052142>
- 539 [44] Kamińska, A. M., Strąkowski, M. R., & Pluciński, J. (2020). Spectroscopic Optical Coherence Tomography
 540 for Thin Layer and Foil Measurements. *Sensors*, 20(19), 5653. <https://doi.org/10.3390/s20195653>
- 541 [45] Ametek (2020). *Temperature calibrator Ametek ETC-400A specification*.
 542 <https://www.testequipmentdepot.com/ametek/temperaturecalibrator/etc400a.htm>
- 543



Katarzyna Karpienko was born in Suwałki, Poland in 1987. She received a B.Sc. degree in electronic engineering and telecommunication from Gdańsk University of Technology, Gdańsk, Poland, in 2012 and an M.Sc. degree in electronic engineering and telecommunications in 2013 from the same university. In 2018, she obtained a Ph.D. in technical sciences for work in the field of fiber optic sensors. Her

research is focused on the application of optical methods in medicine.



Marcin J. Marzejon was born in Tczew, Poland, in 1993. He received the M.Sc. (2017) degree from Gdańsk University of Technology (GUT), Poland. In 2018, he joined the Physical Optics and Biophotonics Group at the Institute of Physical Chemistry PAS, led by prof. Maciej Wojtkowski. He is currently pursuing the Ph.D. degree in the Department of Metrology and Optoelectronics, GUT. His research

activity is focused on the application of optics in biology and medicine.



Adam Mazikowski (born in 1971) received the master's degree in Electronic Equipment Design in 1995 from Gdańsk University of Technology. In 2003 he received Ph.D. degree in optoelectronics from the Gdańsk University of Technology, Faculty of Electronics, Telecommunication and Informatics, Gdańsk, Poland. From 1995 to 2003, he was Research Assistant and since 2003, he has been Assistant

Professor with the Department of Metrology and Optoelectronics, Gdańsk University of Technology, Poland. His research interests include non-contact emissivity and temperature measurement, optoelectronic sensors (incl. biomedical sensors), optoelectronic displays, photometry and colorimetry, and virtual reality systems.



Jerzy Pluciński (born in 1960) received an M.Sc. degree in electronics from the Faculty of Electronics, Gdańsk University of Technology, Poland in 1984, and then in 1994, obtained his Ph.D. degree in optoelectronics (summa cum laude). In 2010, he obtained Habilitated Doctor degree (summa cum laude) from the same university. His research interests are optoelectronics and photonics, optics of highly

scattering materials, optical coherence tomography, optical fiber sensors, and laser technology. He has authored or co-authored over 150 scientific papers, 2 books, and 3 book chapters. Now he is Professor at Gdańsk University of Technology, Poland.